Materials Advances

ROYAL SOCIETY OF CHEMISTRY

PAPER

View Article Online
View Journal | View Issue

Cite this: *Mater. Adv.*, 2024, 5, 5845

Copper-based core–shell metamaterials with ultra-broadband and reversible ENZ tunability†

Anastasiia Zaleska,* Alexey V. Krasavin, Anatoly V. Zayats and Wayne Dickson

The inexpensive fabrication of large-area plasmonic nanostructures is essential for the timely technological exploitation of plasmonic phenomena in diverse fields, from photocatalysis to sensitive biological and chemical sensing. Self-assembled porous alumina templates offer such an inexpensive and scalable route to the fabrication of metamaterials, with the ability to cover macroscale areas while retaining nanometric control over the constituent dimensions. Traditionally employing gold and silver, metamaterials have often overlooked less expensive but highly functional transition metal alternatives. Copper presents an interesting metamaterial constituent due to its cost, abundance, intrinsic optical properties and established use as a catalyst, with applications for both metallic copper and its main oxidation states (Cu_2O and CuO). In this work, we have fabricated plasmonic metamaterials comprised of an array of copper nanorods with controllable dimensions with optical properties determined by the geometry of the nanorod array and the formation of copper oxide shells on the nanorods. The high refractive index sensitivity of these metamaterials enabled the complex electrochemistry of copper to be monitored *via in situ* visible light spectroscopy during cyclic voltammetry in a sodium hydroxide solution and the subsequent correlation of the optical spectra with the oxidation and reduction processes. Anodising the metamaterial at a fixed potential enables the controllable and reversible growth of a nanometric shell of copper oxide, at growth rates of approximately 0.23 nm min^{-1}, confirmed by *in situ* optical spectroscopy and electromagnetic simulations. This not only introduces an additional mechanism for broad spectral tuning of the epsilon-near-zero spectral range and the corresponding extinction peak by >100 nm, but also provides a scalable method to fabricate designer core–shell metamaterials with new functionalities.

Received 15th December 2023,
Accepted 15th May 2024

DOI: 10.1039/d3ma01129a

rsc.li/materials-advances

1 Introduction

The recent drive to exploit plasmonic hot-carrier effects in sensing and photocatalysis has caused an upsurge in the development of new material approaches in plasmonics and a drift away from the traditional plasmonic noble metals.[1–5] In the past few years, this has led to a wide search for alternative plasmonic media that are either inexpensive or provide additional functionalities. Copper, as one such alternative plasmonic constituent, benefits from both high natural abundance and low cost, making it an intrinsically attractive material for commercial exploitation. In particular, copper electrodes have been used as efficient electrocatalysts for reactions such as CO_2 reduction,[6–11] water splitting,[12–15] self-cleaning[9,16] and plasmon-induced organic transformations.[17,18]

In this paper, for the first time, we introduce a new plasmonic metamaterial based on an array of copper nanorods with ultrabroad and reversible ENZ tunability, engineered by taking advantage of nanoscale electrochemical oxidation and reduction of the nanorod surface over the macroscale array ($\approx$1 cm^2 and $\approx 10^{11}$ nanorods). Herein, we describe the fabrication method as well as the structural and optical characterisation of highly uniform large-area copper-based plasmonic metamaterials. These metamaterials are fabricated using anodic aluminium oxide (AAO) as a template.[19,20] This technique has considerable advantages in terms of scalability, whilst also providing both nanometric control of the constituents and high uniformity, resulting in broad spectral tunability of the resonant modes and plasmonic functionality.[21–23]

Beyond the well-known application of copper as an efficient catalyst, copper (as well as silver) nanomaterials are often at a disadvantage for more traditional plasmonic applications compared to those produced using noble metals due to the

Department of Physics and London Centre for Nanotechnology, King's College London, Strand, London WC2R 2LS, UK. E-mail: anastasiia.zaleska@kcl.ac.uk

† Electronic supplementary information (ESI) available: Simulation details along with an additional study of optical properties of metamaterial in different surrounding media, permittivities for copper and its oxidation states with further fabrication details are presented in the ESI. See DOI: **https://doi.org/10.1039/d3ma01129a**

potential for oxidation. In more recent work, oxidation has been addressed by coating the Cu nanomaterials with various passivation layers deposited by atomic layer deposition (ALD).[24] However, the oxides of copper are also well-established photo- and electrocatalysts,[25–29] and the results of our work have resulted in the development of bespoke core–shell Cu/Cu_xO light harvesting metamaterials with nanometrically controllable dimensions and designer optical properties. Here, we describe the procedure for the controllable growth and reduction of copper oxide layers of nanometric thickness *via* electrochemical oxidation in an alkaline electrolyte. This process was monitored in real-time using *in situ* visible light spectroscopy and the results were validated using numerical modelling. Furthermore, optical spectra were obtained in real-time during cyclic voltammetry and correlated with the electrochemical processes. This methodology presents the opportunity to combine the catalytic functionality of copper and its oxides with plasmonic light harvesting and catalytic enhancement in high surface area metamaterials.

2 Results and discussion

2.1 Fabrication and optical characterisation of copper nanorod metamaterials

The fabrication process begins by magnetron sputtering 10 nm of tantalum pentoxide (Ta_2O_5) onto a 0.7 mm thick glass (SiO_2) substrate to act as an adhesion layer. This is followed by the sputter deposition of 8 nm of gold (Au) and finally 280 nm of aluminium (Al) (Fig. 1a). The aluminium is then electrochemically anodised at 1 °C in a sulphuric acid (H_2SO_4) solution at an applied constant voltage of 25 V, which results in formation of a porous AAO matrix. The barrier layer formed at the bottom of the pores was removed by etching in a 30 mM sodium hydroxide (NaOH) solution, which provides access to the underlying gold layer serving as an electrode for subsequent electrodeposition. In addition to the removal of the barrier layer, the duration of this etching step determines the final diameter of the pores and provides geometrical control that translates into spectral tunability of the optical properties of the final metamaterial.[20] For further fabrication details see the Methods section.

In order to form the final plasmonic metamaterial, copper was electrodeposited into the pores of the alumina template from a 0.12 M copper sulfate ($CuSO_4$) solution mixed with 0.49 M H_3BO_3 under a constant voltage of −2.8 V. Electrodeposition was carried out at room temperature in a custom-made electrochemical cell consisting of a three-electrode configuration, with platinum (Pt) foil as a counter electrode and a silver–silver chloride (Ag/AgCl) reference electrode. Fig. 1b and c show SEM images of a uniform array of vertically-aligned copper nanorods before and after the removal of the alumina template *via* chemical etching in 0.3 M NaOH. The length of the metallic nanorods comprising the metamaterial is determined by the electrodeposition duration and can be varied from 30 nm to the limiting value dictated by the thickness of the porous AAO (typically 275–400 nm). Energy-dispersive X-ray spectroscopy analysis (EDX), confirmed an abundance of copper and the elemental composition in the metamaterial architecture.

The optical properties of the fabricated metamaterials are determined by polarisation-resolved visible light spectroscopy. Experiments were performed in transmission using both TM- and TE-polarised light at various angles of incidence. Fig. 2 shows the experimental extinction spectra of copper nanorods embedded in the alumina matrix as a function of the angle of incidence for both polarisations. The optical properties revealed are those typical for such anisotropic uniaxial metamaterials,

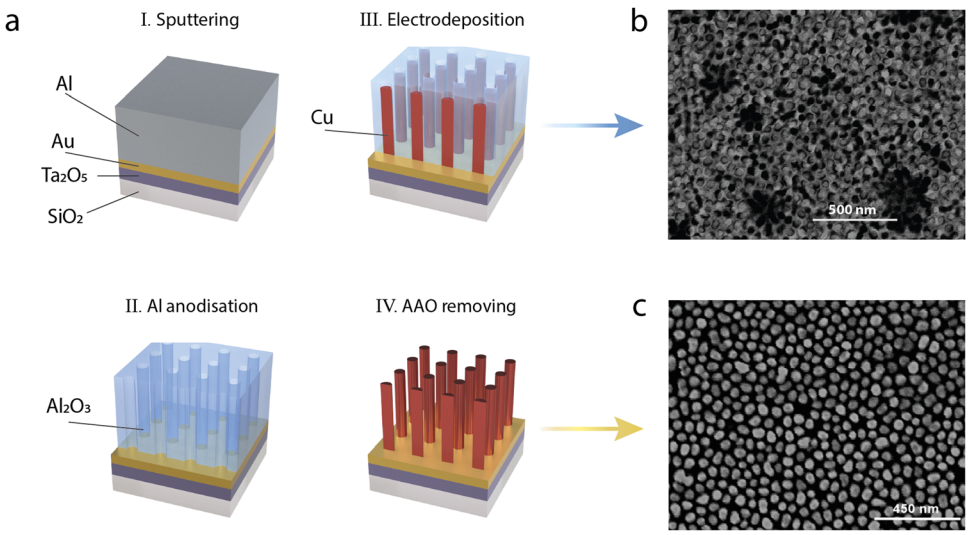

Fig. 1 (a) A schematic diagram of the fabrication steps to form arrays of copper nanorods using AAO templates. (I) The formation of thin multilayer films by magnetron sputtering, (II) the anodisation of aluminium to create a porous AAO template and consequential removal of the barrier layer, (III) the electrodeposition of copper into the alumina pores, (IV) the Cu nanorods exposed to air after the removal of the AAO. Top-view SEM images of the resulting array of copper nanorods (b) before and (c) after complete removal of the alumina using 0.3 M NaOH.

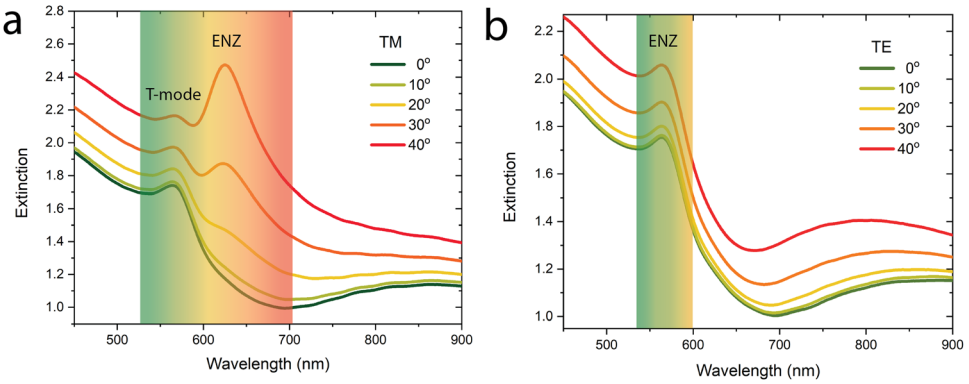

Fig. 2 Measured extinction spectra of Cu nanorod arrays embedded in an alumina matrix under (a) TM- and (b) TE-polarised light illumination at various angles of incidence. The metamaterials are comprised of nanorods with 17 nm radius, 220 nm length, and a mean centre-to-centre separation of 85 nm.

exhibiting two extinction peaks.[30] Under normal incidence illumination, the short-wavelength peak, present at a wavelength of approximately 570 nm, is related to the excitation of a transverse dipolar plasmonic resonance of the nanorod metal core (T-mode). Increasing the angle of incidence and using TM polarised light reveals a second extinction peak at 620 nm, associated with the high attenuation of the TM mode inside the metamaterial in the epsilon-near-zero (ENZ) regime when the effective component of the permittivity perpendicular to the substrate (parallel to the long axis of the nanorods) is close to zero (see Methods for the description of metamaterial effective optical properties). The spectral width of the ENZ peak (and hence damping) does not differ significantly with respect to that observed for gold nanorod-based metamaterials with a similar nanoscale geometry.[30] The position of the ENZ extinction peak (in particular) may be tuned throughout the visible spectrum by varying the dimensions of the individual rods (Fig. S1, ESI†). At the same time, the spectral position of the ENZ peak, together with that of thickness-dependent resonances appearing in the metamaterial slab is determined by the electromagnetic coupling between the nanorods affected by the surrounding refractive index, making such metamaterials particularly suitable for sensing applications (Fig. S2, ESI†).[22,31,32]

2.2 The electrochemistry of Cu metamaterials

2.2.1 Cyclic voltammetry and *in situ* optical spectroscopy.

The sensitivity of the metamaterial's spectral response to changes in the refractive index can provide a route to efficient engineering of the optical properties. An attractive route to accomplish this is the electrochemical anodisation of copper using NaOH. This method facilitates the creation of either a Cu_2O or a CuO shell, providing nanometric control over the thickness of the oxide layer. It is also inexpensive and in keeping with the scalable nature of the overall fabrication process.

Prior to all electrochemical studies, the alumina matrix surrounding the nanorods was removed using a NaOH solution (0.3 M NaOH for approximately 5 minutes) revealing arrays of free-standing nanorods, conductively connected *via* the remaining gold underlayer. A custom-made three-electrode electrochemical cell was used, comprising a platinum counter electrode, a saturated Ag/AgCl reference electrode and a 0.15 M NaOH electrolyte with the copper nanorod metamaterial serving as the working electrode. The optical properties of the metamaterials were continuously monitored using *in situ* transmission spectroscopy (200 ms per spectrum) with TM polarised light at an incident angle of 40°, allowing both extinction peaks to be observed. First, cyclic voltammetry (CV) was performed for five cycles in the potential range of Cu_2O and CuO formation at a sweep rate of 0.01 V s^{-1} in order to confirm the presence and position of the oxidation and reduction peaks and the stability of the nanostructures over cycling (Fig. S3, ESI†). The material was initially precycled to obtain a stable CV scan.

Fig. 3a shows the corresponding cyclic voltammogram after one cycle, verifying the potential for the formation of Cu_2O at −0.38 V (designated A_1) and a broad anodic peak at a maximum of +0.06 V (designated A_2) corresponding to further Cu(I) to Cu(II) oxidation. Both the oxidation and reduction peaks can be clearly identified as expected from the literature[33–35] and the results obtained for a previously anodised copper thin film (Fig. S4, ESI†).

The optical properties of the metamaterial during the CV sweep are summarised in Fig. 3b–e. The colours overlayed on the cyclic voltammogram (yellow, green, blue and pink) correspond to the four oxidation/reduction reactions occurring at the surface of the copper nanorods. The experimental extinction spectra measured during one cycle of the CV sweep are thus divided into four plots (Fig. 3(b)–(e)) to illustrate how the optical properties of the sample evolve through each stage of the process. The border of each set of extinction spectra is coloured to match the highlighted regions in the CV sweep. Additionally, the colour of the curves in each plot corresponds to the coloured circular markers at specific points in that section of the CV sweep, showing the direction of transition of the optical properties (also indicated by arrows). These markers are located at the starting potential (0 V) and each key oxidation/reduction peak.

The extinction spectrum of the metamaterial is initially characterised by a single peak (Fig. 3b, red curve), as the transverse resonance and ENZ extinction regions overlap in

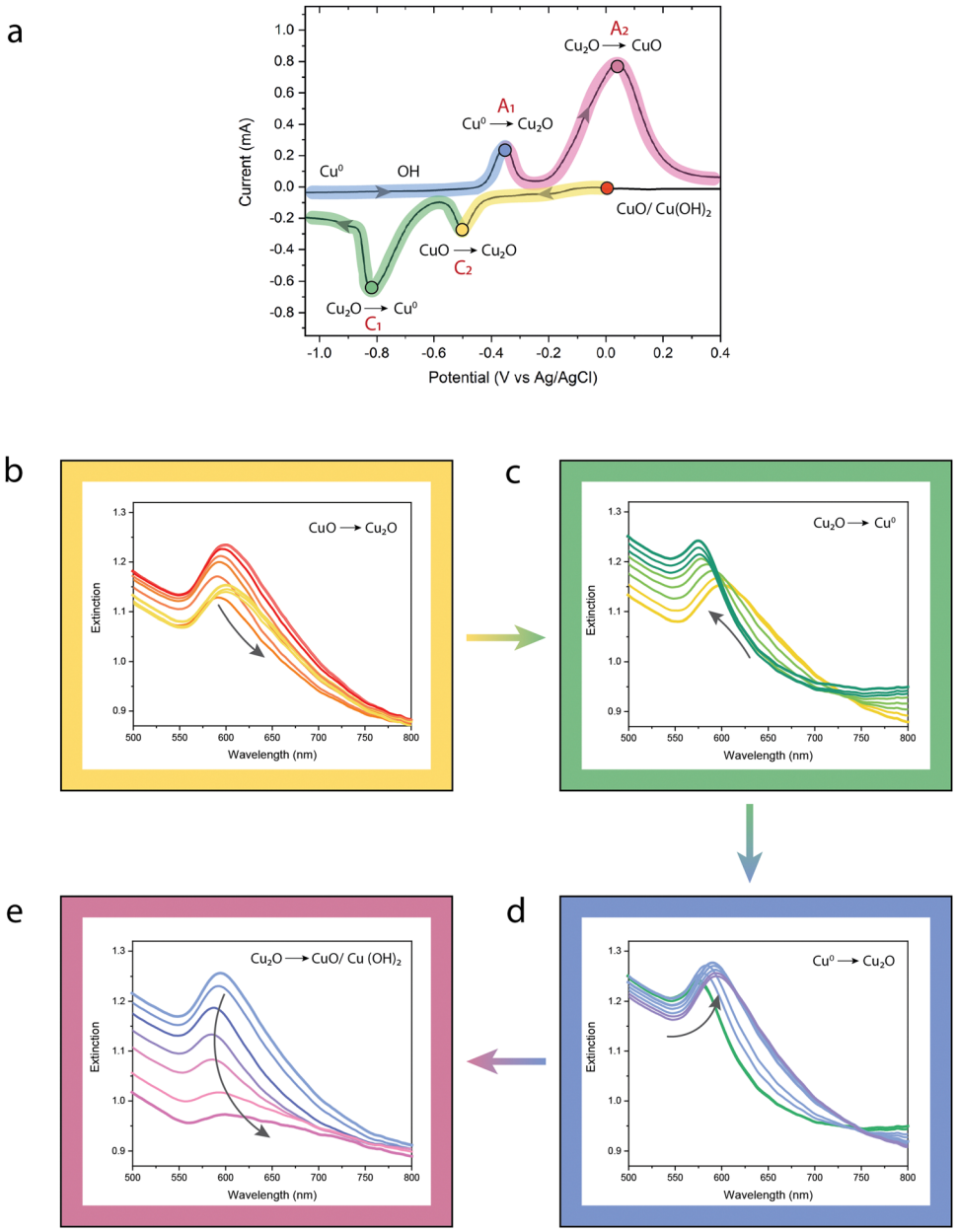

Fig. 3 The study of the optical response of a copper nanorod electrode in a 0.15 M NaOH within a (a) CV sweep at a scan rate of 0.01 V s^{-1}. Colour points are positioned on the reduction/oxidation peaks (b)–(e). Each set of extinction spectra transition from one coloured point on the CV chart to another, with the beginning and end points are designated by bold lines of the same colour. Each spectrum is labelled with its respective concluding reaction. The parameters of the copper nanorod metamaterial are 180 nm length, 23 nm radius and 80 nm period.

wavelength, which is typical for this architecture of nanorod metamaterial with these dimensions (a 23 nm diameter, an 80 nm spacing) in an aqueous solution ($n \sim 1.33$). In addition, the broad width of the extinction peak is the result of a mixed oxide/hydroxide surface following previous CV sweeps.

Our analysis of the *in situ* spectroscopy begins at a potential of 0 V *vs.* Ag/AgCl at the beginning of the reductive cathodic sweep. As the potential decreases towards cathodic peak C_2 (Fig. 3a) located at a potential of −0.31 V *vs.* Ag/AgCl, a non-monotonous change in the extinction maximum is observed (Fig. 3b). At low negative potentials, this is characterised by both a blue-shift of the extinction peak and a decrease in its magnitude. This may be explained by the decomposition of dissolved $Cu(OH)_4^{2-}$ to CuO,[36] increasing the losses due to the large imaginary component of the dielectric constant of CuO (Fig. S5, ESI†). However, as the potential reaches C_2, this behaviour is reversed, and Fig. 3b shows a red-shift of the peak and an increase in its magnitude. This region of the sweep and peak C_2 in particular is assigned to the partial reduction of CuO to Cu_2O,[37] while the red-shift of the extinction peak and increase in its magnitude are characteristics of the change in the dielectric permittivity of Cu_2O having a larger real and a

lower imaginary components in this spectral range, compared to CuO (Fig. S5, ESI†). At more negative potentials towards peak C_1 a series of concurrent reduction processes, consisting of the reduction of Cu^{2+} species and Cu_2O to metallic Cu, take place. This is readily observed in the extinction spectra shown in Fig. 3c, where there is a dramatic increase of the magnitude of the extinction peak together with a blue-shift in its spectral position. The increase in extinction is a result of the reduction of any remaining (lossy) CuO/Cu_2O and an increase in the metallic content of the nanorods. In this scenario, the transverse resonance would experience a blue-shift due to the lower effective dielectric constant surrounding the metal core. For the ENZ extinction peak, the blue-shift is a result of the increase in the metal filling factor (f in eqn (3)) with a commensurate decrease in the dielectric constant surrounding the nanorods. From the perspective of the nanorods in the array, each nanorod experiences a decrease in the surrounding dielectric constant, their aspect ratio decreases and the dipolar coupling increases between adjacent rods – all contributing to the observed blue-shift.

As the anodic sweep begins, the nanorods are comprised entirely of metallic copper. As the potential is increased from −1.2 V *vs.* Ag/AgCl, the surface first becomes hydroxylated, with the formation of $Cu(OH)_2$, before reaching anodic peak A_1 located at a potential of −0.35 V *vs.* Ag/AgCl where the formation of Cu_2O takes place (Fig. 3d).[38] Examination of Fig. 3d shows that as the potential increases and the formation of Cu_2O begins, creating Cu/Cu_2O core–shell nanorods, there is a distinct red-shift and broadening of the main extinction peaks. The explanation is precisely the reverse of that described for peak C_1 above: an increase in the effective dielectric constant surrounding the nanorods *via* the growth of Cu_2O and a decrease in the diameter of the metallic nanorods (and hence the metal filling fraction inside the nanorod η). Despite the red-shift primarily affecting the ENZ extinction peak as we shall see later in the manuscript, two distinct peaks are not observed, mainly due to the small magnitude of the red-shift (~30 nm) and the optical loss intrinsic to Cu_2O at this wavelength compared with the aqueous electrolyte. Further increasing the potential towards peak A_2 results in a dramatic transformation of the extinction spectrum (Fig. 3e), as first the formation of $Cu(OH)_4^{2-}$ and $Cu(OH)_2$ takes place (up-slope) followed by potential oxidation to CuO.

The reduction in the overall extinction and dramatic broadening of the peak may be explained once again by comparing the relative permittivity of Cu_2O and CuO, the latter characterised by a significantly lower real part of epsilon and an order of magnitude higher imaginary component at a wavelength of 600 nm (Fig. S5, ESI†). Despite the paucity of data on the refractive index of copper hydroxides, the general behaviour of the extinction spectra is qualitatively reproduced by numerical modelling of a Cu/CuO core–shell system with various CuO shell thicknesses (Fig. S6, ESI†). The situation is further complicated as the voltage increases following peak A_2, as the slow hydroxylation of CuO to soluble $Cu(OH)_4^{2-}$ is expected to occur.[36] However, recent work by Topali *et al.*[39] claims there is little evidence of CuO formed *in situ*, and instead of the often stated $CuO/Cu(OH_2)$ duplex layer formed following anodic peak A_2[40] a complex mixed oxide/hydroxide layer containing metastable Cu_4O_3 is formed, with the latter becoming CuO following removal from the electrolyte. The precise composition of the film cannot be determined from the measurements here, as the dielectric permittivity of Cu_4O_3 at a wavelength around 600 nm while significantly different to that of CuO, also has a larger imaginary component than Cu_2O (Fig. S7, ESI†), which could result in a similar spectral shape, depending on the exact layer thicknesses and hierarchical distribution of the different oxides. Further detailed analysis of the composition in this complex region is beyond the aim and scope of this work.

2.3 Oxidation and reduction

2.3.1 Anodisation of Cu nanorods. With an aim to electrochemically form core–shell nanorods comprised of a metallic Cu core and a Cu(I) oxide shell (Fig. 4a), anodisation was carried out at −0.39 V *vs.* Ag/AgCl in a custom-made electrochemical cell filled with a 0.15 M NaOH electrolyte solution. During the anodisation process, the copper metamaterial was illuminated at an incident angle of 40° with TM-polarised light for transmission measurements. The colour plot in Fig. 4a is obtained from the experimentally acquired *in situ* extinction spectra at various anodisation times and therefore increasing thickness of the Cu_2O shell. The transverse resonance and ENZ extinction peaks can be clearly observed and are initially located at wavelengths of 600 nm and 700 nm respectively. As the anodisation proceeds, there is a significant red-shift of the ENZ peak. This behaviour is as expected for similar reasons as discussed previously: a small shift of the T-mode due to the higher refractive index of the Cu_2O shell, while a much larger red-shift of the ENZ peak is observed due to the corresponding shift of the ENZ point.

To confirm the observations in Fig. 4a, further aid understanding the optical behaviour of the core–shell Cu/Cu_2O metamaterials, and gain an insight into the thicknesses of the created oxide layers, the extinction spectra were calculated as a function of the Cu_2O shell thickness using full-vectorial simulations of a square nanorod array (for details see Methods). Fig. 4b shows the resulting extinction calculated as a function of the Cu_2O shell thickness on a copper nanorod surface under plane-wave illumination with TM-polarised light at 40° incidence. The dimensions used in the simulations matched the fabricated nanomaterials, with the initial and final geometrical parameters (diameter, length) obtained from SEM and AFM images. The anodisation process was simulated to include the consumption of the metallic Cu and formation of Cu_2O as well as the volume expansion caused by the oxidation. The volume expansion was estimated to be approximately 30% which is in agreement with previous measurements performed on a freshly formed Cu(I) oxide layer of a similar thickness on a copper film. As observed experimentally, the calculations in Fig. 4b show the ENZ extinction peak undergoing a red-shift as the thickness of the Cu_2O is increased. Due to the lack of material inhomogeneity in the simulation, the linewidth of the peaks is appreciably narrower,

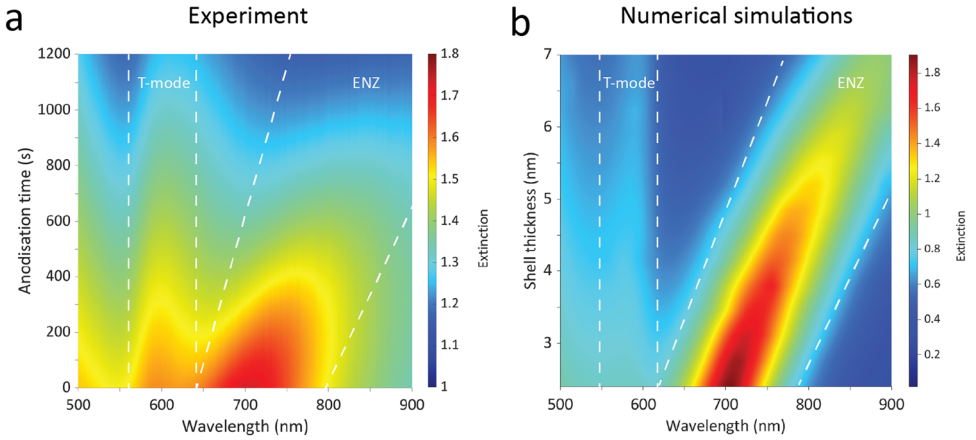

Fig. 4 (a) The measured extinction spectra during the surface oxidation of the copper nanorod material in a 0.15 M NaOH electrolyte solution at −0.39 V *vs.* Ag/AgCl. (b) The calculated extinction spectra as a function of the shell thickness of Cu_2O with the increase of the aspect ratio. All extinction spectra were acquired at an incident angle of 40° using TM polarised light. The initial parameters of the copper nanorods: a 13.2 nm radius, a 188.6 nm length, and an 80 nm period.

despite the simulations using a mean-free restricted path model for the permittivity of Cu. Comparing these results with the experimental spectra shown in Fig. 4a, both the red-shift of the ENZ peak and the reduction of its magnitude are reproduced. Moreover, this analysis allows us to estimate the growth rate of the oxide shell during the anodisation to be 0.23 nm min^{-1}, matching the experimentally measured spectral position of the ENZ peak changing approximately linearly with the anodisation time to the simulated one changing linearly with the oxide Cu_2O thickness (Fig. S8, ESI†). The oxide shell thickness is estimated to exceed 7 nm, dramatically shifting the ENZ extinction peak into the near-IR range. For clarification of the mechanisms underpinning the dramatic wavelength shift, calculations were also performed varying the oxide shell thickness, but maintaining a constant copper nanorod diameter *i.e.* ignoring the reduction in radius due to oxidation. The results are shown in Fig. S9 (ESI†) and, as expected, demonstrate a significantly reduced tunability, highlighting the combination of optical processes contributing to the rapid red-shift observed in the experiment. Additionally, after detaching the core–shell Cu/Cu_2O nanostructures from a glass substrate, the formation of copper oxide shell around the copper nanorod-based metamaterial was revealed using transmission electron microscopy (TEM) and energy dispersive spectroscopy (EDS) mapping, as shown in Fig. S10 (ESI†). This also allowed us to estimate the shell thickness of the formed oxide layer, which was found to be in agreement with the calculated prediction based on the optical response of the metamaterial. The oxidation state of Cu in the fabricated core–shell Cu/Cu_2O nanostructures was analysed by X-ray photoelectron spectroscopy (XPS) confirming their composition (Fig. S11, ESI†).

The extinction spectra of a Cu/CuO core–shell nanorod metamaterial were calculated for comparison and to fully explore the optical properties of these core–shell geometries (Fig. S6, ESI†). Compared to copper oxide, the dielectric permittivity of copper(II) oxide is characterised by a significantly larger imaginary component and a smaller real component at wavelengths above 525 nm. The large imaginary component is responsible for additional broadening of the ENZ extinction peak as the thickness of the copper(II) oxide shell is increased, and indeed it is not discernible in the calculated spectra until the shell reaches 5 nm in thickness at which point the ENZ peak is red-shifted to a wavelength greater than approximately 800 nm where the imaginary component of the permittivity of CuO begins to decrease significantly (Fig. S5, ESI†).

2.3.2 Reversibility. The oxidation process shown in Fig. 4 illustrates the ability to create core–shell (Cu/Cu_2O) heterostructured nanorods *via* electrochemical oxidation, which provides nanometric control of the Cu_2O shell thickness. Another

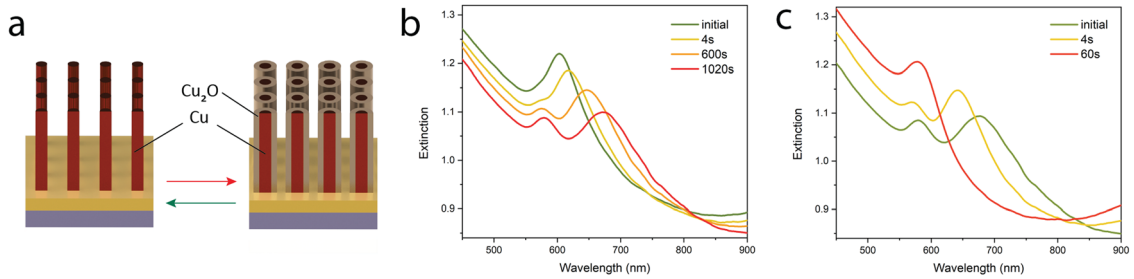

Fig. 5 (a) The schematics of electrochemical formation of copper oxide on the Cu nanorod surface. The measured extinction spectra during (b) the oxidation and (c) the reduction of the copper electrode for 20 minutes in an electrochemical cell with a 0.15 M NaOH solution.

major benefit of creating such heterostructures electrochemically is that this oxide may be subsequently reduced. The reversibility of the oxidation process is demonstrated in Fig. 5a. Fig. 5b shows extinction spectra during the formation of the Cu_2O shell, which as expected, rapidly induces a red-shift of the ENZ wavelength, with approximately a 20 nm shift occurring within the first 10 s. As the anodisation process continues, the rate of red-shift reduces due to restricted diffusion through the Cu_2O layer (Fig. 5b). At the end-point of anodisation, the ENZ point reaches a wavelength of approximately 680 nm. As the reduction step proceeds (Fig. 5c), the reversibility is confirmed and the extinction peak rapidly blue-shifts, recovering its initial spectral position and magnitude in less than 60 s. The difference between the initial and final peak positions amounts to approximately 3 nm and may be explained by an initial (thin) oxide coating on the copper nanorods prior to electrochemical oxidation. To confirm the stability of the oxidation and reduction processes, we ran a switching loop over multiple cycles, −0.39 V and −0.87 V *vs.* Ag/AgCl for 6 seconds and 10 seconds, respectively, and observed no appreciable deterioration in the optical properties (Fig. S12, ESI†). In applications of these materials, it would be trivial to remove the native oxide from a copper surface by initially applying the high negative voltage at −0.87 V *vs.* Ag/AgCl. The ability to refresh the copper surface is of considerable benefit for electrocatalytic applications.

3 Conclusions

In this work, we have presented an inexpensive fabrication process for plasmonic metamaterials based on subwavelength arrays of copper nanorods. The method described has considerable advantages in terms of scalability whilst retaining nanometric control of the constituent nanorods which provides broad plasmonic tunability throughout the visible spectrum. The complex electrochemistry of copper in alkaline electrolytes has been studied using the cyclic voltammetry combined with *in situ* optical spectroscopy to interrogate the optical properties of the metamaterial. The extraordinary refractive index sensitivity displayed by metamaterials of this architecture provides a unique method to monitor the surface composition in real-time, which together with other techniques, can help to provide new insights into the complex electrochemical processes. The anodisation of copper in alkaline solutions offers a route to the scalable synthesis of core–shell Cu–Cu_xO nanorod metamaterials. The anodisation of the copper is highly controllable and reversible, with the oxidation rate estimated to be approximately 0.23 nm min^{-1}, enabling the fabrication of ultrathin shells of copper oxides with sub-nanometer precision. Using this process, a reversible spectral shift of >100 nm has been demonstrated for the ENZ extinction peak. This spectral shift is only constrained by the initial dimensions of the nanorods comprising the metamaterial. The implemented fabrication process provides a novel route to both tune the optical properties of the metamaterial and more importantly, create functional oxide surfaces of controllable thickness for the development of highly efficient plasmonic photocatalysts and sensitive sensors.

Specifically, with regard to the photo and photo-electrocatalytic reduction of CO_2, the copper-based metamaterials developed here have the properties to be considered excellent candidates as they provide the high surface area, excellent light absorption, refractive index-based monitoring of the catalytic surface, the potential for SERS monitoring of adsorbed surface species[41] while the ability to electrically address the copper constituents also enables electrocatalytic surface modification and restructuring for enhanced efficiency and designer specificity.[42] We expect that Cu/Cu_2O core–shell nanomaterials may be more durable, with their stability depending on the thickness of the anodised oxide layer.

4 Methods

4.1 Fabrication details

Magnetron sputtering (The Kurt J. Lesker Company PVD75 Sputter System) was used as the deposition method for the production of the multilayer thin films on transparent glass substrates (Corning Eagle XG, uncoated) composed of tantalum pentoxide (Ta_2O_5, 99.95% purity), gold (Au, 99.99%) and aluminium (Al, 99.99%). Previous ellipsometry measurements confirmed the presence of stoichiometric Ta_2O_5, which had been detected by low absorption in the visible spectrum.[43] The anodisation process was performed at 2 °C in a specifically designed electrochemical cell filled with a 0.3 M H_2SO_4 electrolyte solution. A constant voltage of 25 V was applied between the sample (anode) and the Pt foil as a counter electrode (cathode). The anodised samples were subsequently etched in 30 mM NaOH to achieve pore widening and to remove the barrier layer. Copper electrodeposition was performed with a three-electrode system at an applied voltage of −2.8 V using a 0.12 M copper sulphate ($CuSO_4$) solution mixed with 0.49 M H_3BO_3. The length of the nanorods was controlled with the electrodeposition time. The sample was etched in 30 mM NaOH to remove the AAO matrix and expose the metamaterial to air.

4.2 Characterisation techniques

All scanning electron microscopy images were taken with a Zeiss EVO LS15 Scanning Electron Microscope with Oxford Instruments Energy-Dispersive X-Ray Spectroscopy systems. The images were processed with ImageJ. TEM images were obtained with a JEOL JEM F200 transmission electron microscope.

Optical spectroscopy was performed in a custom-built system using plane-polarised, collimated white light from a tungsten-halogen lamp. After passing through the sample, the light was collected by an objective lens and coupled to a spectrometer (Ocean Optics QE Pro) *via* a multimode optical fibre. To investigate the linear optical properties of nanostructures, transmission spectra in various surrounding media were acquired as functions of the angle and polarisation of the incident light. The electrochemical oxidation process was

continuously monitored in real-time in transmission using *in situ* visible light spectroscopy spectroscopy (200 ms per spectrum) with TM polarised light at an incident angle of 40°.

4.3 Effective medium theory of a nanorod-based metamaterial

As the nanorod diameter is much smaller than the wavelength, the effective optical properties of square or randomly distributed 2D arrays of oriented nanorods are calculated using effective medium theories in the long-wavelength (quasi-static) limit within the Maxwell Garnett approximation.[44,45] Each nanorod is considered to be in a field produced by the illuminating wave and the averaged field generated by all other nanorods. The effective dielectric permittivity of a metamaterials in this case is calculated by averaging the overall electric and electric displacement fields.

$$\langle \mathbf{D} \rangle = \boldsymbol{\epsilon}_{\mathrm{eff}} \langle \mathbf{E} \rangle. \quad (1)$$

Due to its symmetry, the nanorod array behaves as a highly anisotropic uniaxial medium with the permittivity in the major axes given by a diagonal tensor $\boldsymbol{\epsilon}_{\mathrm{eff}} = (\epsilon_{\mathrm{eff},\perp}, \epsilon_{\mathrm{eff},\perp}, \epsilon_{\mathrm{eff},\parallel})$, with effective permittivity components perpendicular ($\perp$) and parallel ($\parallel$) to the optical axis directed along the nanorods. Using eqn (1) and carefully averaging **E** and **D** along the major axes one obtains the following expressions for the permittivity components:[45]

$$\epsilon_{\mathrm{eff},\perp} = \frac{\epsilon_{\mathrm{m}} + f[\alpha_{\mathrm{c}}\eta\epsilon_{\mathrm{c}} + \alpha_{\mathrm{s}}(1-\eta)\epsilon_{\mathrm{s}} - \epsilon_{\mathrm{m}}]}{1 + f[\eta\alpha_{\mathrm{c}} + \alpha_{\mathrm{s}}(1-\eta) - 1]}, \quad (2)$$

where

$$\alpha_{\mathrm{c}} = \frac{4\epsilon_{\mathrm{m}}\epsilon_{\mathrm{s}}}{(\epsilon_{\mathrm{c}} + \epsilon_{\mathrm{s}})(\epsilon_{\mathrm{s}} + \epsilon_{\mathrm{m}}) + \eta(\epsilon_{\mathrm{c}} - \epsilon_{\mathrm{s}})(\epsilon_{\mathrm{s}} - \epsilon_{\mathrm{m}})},$$

$$\alpha_{\mathrm{s}} = \frac{2\epsilon_{\mathrm{m}}(\epsilon_{\mathrm{c}} + \epsilon_{\mathrm{s}})}{(\epsilon_{\mathrm{c}} + \epsilon_{\mathrm{s}})(\epsilon_{\mathrm{s}} + \epsilon_{\mathrm{m}}) + \eta(\epsilon_{\mathrm{c}} - \epsilon_{\mathrm{s}})(\epsilon_{\mathrm{s}} - \epsilon_{\mathrm{m}})};$$

and

$$\epsilon_{\mathrm{eff},\parallel} = f[\eta\epsilon_{\mathrm{c}} + (1-\eta)\epsilon_{\mathrm{s}}] + [1-f]\epsilon_{\mathrm{m}}, \quad (3)$$

where ϵ_{c}, ϵ_{s} and ϵ_{m} are the permittivities of the core, shell and the dielectric matrix, respectively, f is the nanorod filling factor inside the unit cell (in the case of a square nanorod arrangement equal to $\pi(r_{\mathrm{c}} + t_{\mathrm{s}})^2/a^2$) and $\eta = r_{\mathrm{c}}^2/(r_{\mathrm{c}} + t_{\mathrm{s}})^2$ is the core filling factor inside the nanorod, with r_{c} being the radius of the core, t_{s} the thickness of the shell and a the array spacing. With an absence of artificial magnetic response in the nanorods and zero material magnetism at optical frequencies $\mu_{\mathrm{eff}} = 1$.

4.4 Modelling of the optical response of Cu-based metamaterials

Numerical modelling was performed using 3D finite-element-method simulations in a frequency domain using the commercial software package (CST Microwave Studio). The plasmonic system was represented as an idealised square array. Taking advantage of the symmetry of the structure, a unit cell of the array was modelled, with periodic boundary conditions having the proper phase shift defined by the incident angle set on its side boundaries. The incident plane electromagnetic wave was generated using a top port boundary condition, which also ensures the absence of back-reflection from this face. A similar port, but without plane-wave excitation was set at the bottom. The optical constants (n and k) for copper oxides, CuO and Cu_2O, were taken from ref. 46 (Fig. S5, ESI†), the refractive index of the surrounding electrolyte solution is practically equal to that of water and was taken to be 1.33. The optical properties of copper presented in Fig. S13 (ESI†) were taken from tabulated experimental data[47] and corrected by setting the electron mean free path to 3.3 nm,[30,48] which takes into account the highly polycrystalline nature of copper due to the employed electrodeposition fabrication process. The optical properties of Au, Al_2O_3, Ta_2O_5 and SiO_2 were taken from ref. 47 and 49–51 respectively.

Conflicts of interest

There are no conflicts to declare.

Acknowledgements

This work was supported by the UK EPSRC projects EP/M013812/1 and EP/W017075/1. The authors gratefully acknowledge Dr Diptiranjan Paital, Dr William Wardley and Mr William Luckhurst in the Department of Physics and the Centre for Ultrastructural Imaging (CUI) of King's College London for their support and expertise in this work.

References

1 P. Wang, A. V. Krasavin, L. Liu, Y. Jiang, Z. Li, X. Guo, L. Tong and A. V. Zayats, Molecular Plasmonics with Metamaterials, *Chem. Rev.*, 2022, **122**, 15031–15081.
2 M. W. Knight, N. S. King, L. Liu, H. O. Everitt, P. Nordlander and N. J. Halas, Aluminum for Plasmonics, *ACS Nano*, 2014, **8**, 834–840.
3 W. P. Wardley, F. J. Rodrguez-Fortuno, A. V. Zayats and W. Dickson, Improving propagation lengths of ultraviolet surface plasmon polaritons on thin aluminium lms by ion milling, *J. Phys. D: Appl. Phys.*, 2019, **52**, 074004.
4 R. Bower, C. P. T. McPolin, A. V. Krasavin, A. V. Zayats and P. K. Petrov, Temperature stability of individual plasmonic Au and TiN nanodiscs, *Opt. Mater. Express*, 2022, **12**, 3471.
5 A. Y. Bykov, A. Shukla, M. van Schilfgaarde, M. A. Green and A. V. Zayats, Ultrafast Carrier and Lattice Dynamics in Plasmonic Nanocrystalline Copper Sulfide Films, *Laser Photonics Rev.*, 2021, **15**, 2000346.
6 D. Kim, C. S. Kley, Y. Li and P. Yang, Copper nanoparticle ensembles for selective electroreduction of CO_2 to C_2–C_3 products, *Proc. Natl. Acad. Sci. U. S. A.*, 2017, **114**, 10560–10565.
7 X. Zhang, F. Han, B. Shi, S. Farsinezhad, G. P. Dechaine and K. Shankar, Photocatalytic Conversion of Diluted CO_2 into Light Hydrocarbons Using Periodically Modulated

Multiwalled Nanotube Arrays, *Angew. Chem., Int. Ed.*, 2012, **51**, 12732–12735.
8 S. C. Roy, O. K. Varghese, M. Paulose and C. A. Grimes, Toward Solar Fuels: Photocatalytic Conversion of Carbon Dioxide to Hydrocarbons, *ACS Nano*, 2010, **4**, 1259–1278.
9 Q. Zhu, Y. Zhang, J. Wang, F. Zhou and P. K. Chu, Microwave Synthesis of Cuprous Oxide Micro-/Nanocrystals with Different Morphologies and Photocatalytic Activities, *J. Mater. Sci. Technol.*, 2011, **27**, 289–295.
10 C. Janaky, D. Hursan, B. Endrodi, W. Chanmanee, D. Roy, D. Liu, N. R. de Tacconi, B. H. Dennis and K. Rajeshwar, Electro- and Photoreduction of Carbon Dioxide: The Twain Shall Meet at Copper Oxide/Copper Interfaces, *ACS Energy Lett.*, 2016, **1**, 332–338.
11 K. Manthiram, B. J. Beberwyck and A. P. Alivisatos, Enhanced Electrochemical Methanation of Carbon Dioxide with a Dispersible Nanoscale Copper Catalyst, *J. Am. Chem. Soc.*, 2014, **136**, 13319–13325.
12 J. Li, X. Jin, R. Li, Y. Zhao, X. Wang, X. Liu and H. Jiao, Copper oxide nanowires for efficient photoelectrochemical water splitting, *Appl. Catal., B*, 2019, **240**, 1–8.
13 Y. Zhao, W. Wang, Y. Li, Y. Zhang, Z. Yan and Z. Huo, Hierarchical branched Cu_2O nanowires with enhanced photocatalytic activity and stability for H_2 production, *Nanoscale*, 2014, **6**, 195–198.
14 S. Xu and D. D. Sun, Signi cant improvement of photocatalytic hydrogen generation rate over TiO_2 with deposited CuO, *Int. J. Hydrogen Energy*, 2009, **34**, 6096–6104.
15 Z. Zhang and P. Wang, Highly stable copper oxide composite as an e ective photocathode for water splitting via a facile electrochemical synthesis strategy, *J. Mater. Chem.*, 2012, **22**, 2456–2464.
16 S. Sun, X. Song, Y. Sun, D. Deng and Z. Yang, The crystal-facet-dependent e ect of polyhedral Cu_2O microcrystals on photocatalytic activity, *Catal. Sci. Technol.*, 2012, **2**, 925–930.
17 A. Marimuthu, J. Zhang and S. Linic, Tuning Selectivity in Propylene Epoxidation by Plasmon Mediated Photo-Switching of Cu Oxidation State, *Science*, 2013, **339**, 1590–1593.
18 X. Guo, C. Hao, G. Jin, H.-Y. Zhu and X.-Y. Guo, Copper Nanoparticles on Graphene Support: An E cient Photocatalyst for Coupling of Nitroaromatics in Visible Light, *Angew. Chem., Int. Ed.*, 2014, **53**, 1973–1977.
19 R. Atkinson, W. R. Hendren, G. A. Wurtz, W. Dickson, A. V. Zayats, P. Evans and R. J. Pollard, Anisotropic optical properties of arrays of gold nanorods embedded in alumina, *Phys. Rev. B: Condens. Matter Mater. Phys.*, 2006, **73**, 235402.
20 P. Evans, W. R. Hendren, R. Atkinson, G. A. Wurtz, W. Dickson, A. V. Zayats and R. J. Pollard, Growth and properties of gold and nickel nanorods in thin lm alumina, *Nanotechnology*, 2006, **17**, 5746–5753.
21 W. Dickson, G. A. Wurtz, P. Evans, D. O'Connor, R. Atkinson, R. Pollard and A. V. Zayats, Dielectric-loaded plasmonic nanoantenna arrays: a metamaterial with tuneable optical properties, *Phys. Rev. B: Condens. Matter Mater. Phys.*, 2007, **76**, 115411.
22 M. E. Nasir, W. Dickson, G. A. Wurtz, W. P. Wardley and A. V. Zayats, Hydrogen Detected by the Naked Eye: Optical Hydrogen Gas Sensors Based on Core/Shell Plasmonic Nanorod Metamaterials, *Adv. Mater.*, 2014, **26**, 3532–3537.
23 M. E. Nasir, A. V. Krasavin, R. M. Cordova-Castro, C. P. T. McPolin, J. G. Bouillard, P. Wang and A. V. Zayats, Mode Engineering in Large Arrays of Coupled Plasmonic–Dielectric Nanoantennas, *Adv. Opt. Mater.*, 2021, **9**, 2001467.
24 A. S. Preston, R. A. Hughes, T. B. Demille and S. Neretina, Plasmonics under Attack: Protecting Copper Nanostructures from Harsh Environments, *Chem. Mater.*, 2020, **32**, 6788–6799.
25 L. Wan, *et al.*, Cu_2O nanocubes with mixed oxidation-state facets for (photo)catalytic hydrogenation of carbon dioxide, *Nat. Catal.*, 2019, **2**, 889–898.
26 D. Gao, R. M. Aran-Ais, H. S. Jeon and B. Roldan Cuenya, Rational catalyst and electrolyte design for CO_2 electroreduction towards multicarbon products, *Nat. Catal.*, 2019, **2**, 198–210.
27 C. W. Li and M. W. Kanan, CO_2 Reduction at Low Overpotential on Cu Electrodes Resulting from the Reduction of Thick Cu_2O Films, *J. Am. Chem. Soc.*, 2012, **134**, 7231–7234.
28 G. Ghadimkhani, N. R. De Tacconi, W. Chanmanee, C. Janaky and K. Rajeshwar, Efficient solar photoelectrosynthesis of methanol from carbon dioxide using hybrid CuO–Cu_2O semiconductor nanorod arrays, *Chem. Commun.*, 2013, **49**, 1297–1299.
29 Z. Han, R. Kortlever, H. Y. Chen, J. C. Peters and T. Agapie, CO_2 Reduction Selective for C_2 Products on Polycrystalline Copper with N-Substituted Pyridinium Additives, *ACS Cent. Sci.*, 2017, **3**, 853–859.
30 R. J. Pollard, A. Murphy, W. R. Hendren, P. R. Evans, R. Atkinson, G. A. Wurtz, A. V. Zayats and V. A. Podolskiy, Optical Nonlocalities and Additional Waves in Epsilon-Near-Zero Metamaterials, *Phys. Rev. Lett.*, 2009, **102**, 127405.
31 A. V. Kabashin, P. Evans, S. Pastkovsky, W. Hendren, G. A. Wurtz, R. Atkinson, R. Pollard, V. A. Podolskiy and A. V. Zayats, Plasmonic nanorod metamaterials for biosensing, *Nat. Mater.*, 2009, **8**, 867–871.
32 Y. Jiang, A. V. Krasavin, M. E. Nasir, P. Wang and A. V. Zayats, Humidity-induced direct modi cation of the optical response of plasmonic nanorod metamaterials, *Opt. Mater. Express*, 2022, **12**, 4574.
33 M. R. Gennero De Chialvo, J. O. Zerbino, S. L. Marchiano and A. J. Arvia, Correlation of electrochemical and ellipsometric data in relation to the kinetics and mechanism of Cu_2O electroformation in alkaline solutions, *J. Appl. Electrochem.*, 1986, **16**, 517–526.
34 F. Caballero-Briones, J. M. Artes, I. Dez-Perez, P. Gorostiza and F. Sanz, Direct Observation of the Valence Band Edge by in Situ ECSTM-ECTS in p-Type Cu_2O Layers Prepared by Copper Anodization, *J. Phys. Chem. C*, 2009, **113**, 1028–1036.
35 A. Bohme, F. Sterl, E. Kath, M. Ubl, V. Manninen and H. Giessen, Electrochemistry on Inverse Copper Nanoantennas: Active Plasmonic Devices with Extraordinarily Large Resonance Shift, *ACS Photon.*, 2019, **6**, 1863–1868.

36 M. Scherzer, F. Girgsdies, E. Stotz, M. G. Willinger, E. Frei, R. Schlogl, U. Pietsch and T. Lunkenbein, Electrochemical Surface Oxidation of Copper Studied by in situ Grazing Incidence X-ray Diffraction, *J. Phys. Chem. C*, 2019, **123**, 13253–13262.

37 S. Dong, Y. Xie and G. Cheng, Cyclic voltammetric and spectroelectrochemical studies of copper in alkaline solution, *Electrochim. Acta*, 1992, **37**, 17–22.

38 S. D. Giri and A. Sarkar, Electrochemical Study of Bulk and Monolayer Copper in Alkaline Solution, *J. Electrochem. Soc.*, 2016, **163**, H252–H259.

39 C. Toparli, A. Sarfraz and A. Erbe, A new look at oxide formation at the copper/electrolyte interface by in situ spectroscopies, *Phys. Chem. Chem. Phys.*, 2015, **17**, 31670–31679.

40 J. Kunze, V. Maurice, L. H. Klein, H.-H. Strehblow and P. Marcus, In situ STM study of the duplex passive lms formed on Cu(111) and Cu(001) in 0.1 M NaOH, *Corros. Sci.*, 2004, **46**, 245–264.

41 H. An, L. Wu, L. D. B. Mandemaker, S. Yang, J. de Ruiter, J. H. J. Wijten, J. C. L. Janssens, T. Hartman, W. van der Stam and B. M. Weckhuysen, Sub-Second Time-Resolved Surface-Enhanced Raman Spectroscopy Reveals Dynamic CO Intermediates during Electrochemical CO_2 Reduction on Copper, *Angew. Chem., Int. Ed.*, 2021, **60**, 16576–16584.

42 H. Tabassum, X. Yang, R. Zou and G. Wu, Surface engineering of Cu catalysts for electrochemical reduction of CO_2 to value-added multi-carbon products, *Chem. Catal.*, 2022, **2**, 1561–1593.

43 V. N. Kruchinin, V. A. Volodin, T. V. Perevalov, A. K. Gerasimova, V. S. Aliev and V. A. Gritsenko, Optical Properties of Nonstoichiometric Tantalum Oxide TaO_x ($x < 5/2$) According to Spectral-Ellipsometry and Raman-Scattering Data, *Opt. Spectrosc.*, 2018, **124**, 808–813.

44 J. Elser, R. Wangberg, V. A. Podolskiy and E. E. Narimanov, Nanowire metamaterials with extreme optical anisotropy, *Appl. Phys. Lett.*, 2006, **89**, 261102.

45 H. Zhang, Y. Shen, Y. Xu, H. Zhu, M. Lei, X. Zhang and M. Xu, Effective medium theory for two-dimensional random media composed of core–shell cylinders, *Opt. Commun.*, 2013, **306**, 9–16.

46 P. Sawicka-Chudy, M. Sibinski, E. Rybak-Wilusz, M. Cholewa, G. Wisz and R. Yavorskyi, Review of the development of copper oxides with titanium dioxide thin-lm solar cells, *AIP Adv.*, 2020, **10**, 010701.

47 P. B. Johnson and R. W. Christy, Optical Constants of the Noble Metals, *Phys. Rev. B: Condens. Matter Mater. Phys.*, 1972, **6**, 4370–4379.

48 P. Lissberger and R. Nelson, Optical properties of thin lm Au–MgF_2 cermets, *Thin Solid Films*, 1974, **21**, 159–172.

49 R. L. Kelly, Program of the 1972 Annual Meeting of the Optical Society of America, *J. Opt. Soc. Am.*, 1972, **62**, 1336.

50 T. J. Bright, J. I. Watjen, Z. M. Zhang, C. Muratore, A. A. Voevodin, D. I. Koukis, D. B. Tanner and D. J. Arenas, Infrared optical properties of amorphous and nanocrystalline Ta_2O_5 thin films, *J. Appl. Phys.*, 2013, **114**, 083515.

51 I. H. Malitson, Interspecimen Comparison of the Refractive Index of Fused Silica, *J. Opt. Soc. Am.*, 1965, **55**, 1205–1209.